-RESEARCH PAPER-

International Journal of Mining and Geo-Engineering

IJMGE

IJMGE 60-3 (2026) 357-365

DOI: 10.22059/IJMGE.2026.410907.595358

# Mapping hydrothermal alteration and gold mineralization in west Ahar using ASTER and Landsat 7

Majid Shahhosseini [a, *] and Faramarz Doulati Ardejani [b]

[a] *Department of Mining Engineering, Arak University of Technology, Arak, Iran.*

[b] *School of Mining, College of Engineering, University of Tehran, Tehran, Iran.*

Article History:

Received: 10 February 2026.

Revised: 15 February 2026.

Accepted: 22 September 2026.

## ABSTRACT

In this study, the capability of ASTER and Landsat 7 ETM+ sensors for alteration mapping at a scale of 1:20,000 and gold mineralization exploration in western Ahar, East Azerbaijan Province, Iran, was evaluated. The study area is composed of pyroclastic rocks, red to purple conglomerates, sandstones, and argillaceous limestones. The pyroclastic units, which host the gold mineralization zone, consist of alternating lapilli tuff, crystal–vitric tuff, lithic tuff, and volcanic rocks such as basaltic–andesitic lavas. To discriminate alteration zones and lithological units, advanced image processing techniques including band ratios, Principal Component Analysis (PCA), and Spectral Angle Mapper (SAM) were applied to the visible and near-infrared (VNIR) and shortwave infrared (SWIR) bands of the ASTER data. Band ratio techniques were also employed for processing Landsat 7 ETM+ data. The remote sensing results were validated through field investigations, petrographic studies, and geochemical analysis of gold. In the ASTER imagery, false color composites (4–6–8 and 7–2–9) effectively discriminated argillic–sericitic alteration, while the band ratio (14/12) optimally enhanced silicic alteration. In the Landsat 7 imagery, the false color composite RGB = B3/B1 – B3/B5 – B5/B7 was suitable for lithological discrimination, and the band ratio (1/3) effectively highlighted iron oxide alteration. The results confirm the effectiveness of the applied image processing methods in alteration mapping and identifying mineralization potentials, with gold grades ranging from 0.021 to 3.128 g/t in the study area.

**Keywords:** *Advanced paceborne Thermal Emission and Reflection Radiometer (ASTER), Landsat 7, Principal component Aalysis, Spectral angel Mmpper, Gold mineralization.*

## 1. Introduction

Gold deposits in Iran are associated with several geological periods, including the Late Proterozoic–Early Cambrian, Late Paleozoic–Early Triassic, Triassic–Jurassic, Late Cretaceous–Paleogene, Tertiary, and Quaternary. Among these, the Tertiary period of the Cenozoic era represents the most active magmatic phase in the geological history of Iran, with manifestations observed throughout the country except for the Kopeh-Dagh zone. Consequently, the term "metallogenic epoch" is commonly attributed to the Pyrenean tectonic event (Eocene–Oligocene). The most diverse and extensive gold mineralization in Iran formed during the Tertiary. Gold mineralization of the Tertiary period generally occurs within extrusive igneous, pyroclastic, and sedimentary rocks, as well as calc-alkaline (subvolcanic) intrusive rocks and their associated dacitic and andesitic lithologies of Eocene–Oligocene age and younger, particularly during the Miocene–Pliocene. Hydrothermal fluids derived from intrusive igneous bodies penetrated Eocene and Neogene rocks, leading to argillic and silicic alteration and subsequent precipitation of gold and other elements along faults and structural discontinuities. The most significant gold occurrences and deposits of this period include the gold-bearing districts of Kerman, Tarom–Hashtjin, Moallem–Torbat-e Heydarieh (excluding Teknar), Central Iran, Qorveh, and Mianeh, as well as most occurrences and deposits within the Saveh–Kashan–Naein belt, Takab, Arasbaran, and Lut blocks (Ghorbani, 2008). Ten principal zones favorable for gold exploration in Iran have been identified, including Ahar, Mianeh, Takab–Dashkasan, Tarom, Muteh–Astaneh, the Central Iran belt, the Kerman belt, the Mashhad zone, the Kashmar zone, and the Taftan–Ghaleh-Zari zone (Maghsoudi et al., 2005). The study area is located within the Ahar zone, which is considered highly prospective for vein-type copper–gold deposits of Tertiary age (Figure 1). The application of satellite remote sensing data for mapping lithological units and hydrothermal alteration in mineral exploration has expanded significantly in recent years (Sabins, 1999; Yao et al., 2023; Rani, 2025). The ASTER dataset, comprising 14 spectral bands, exhibits strong capability in the shortwave infrared region for identifying diagnostic minerals associated with hydrothermal alteration types, including propylitic, phyllic, argillic, and potassic alterations. Accordingly, ASTER data have been widely utilized in gold mineralization exploration studies (Sheikhrahimi et al., 2019; Gabr et al., 2010; Beiranvand Pour and Hashim, 2012; Bedini, 2019).

Despite significant advances in satellite image processing techniques, gold mineralization exploration based on satellite data has received relatively limited attention. Remote sensing provides a reliable and efficient alternative for identifying hydrothermal alteration halos and prospective zones within the structurally and lithologically complex environments associated with gold mineralization (Sillitoe, 1993). This study aims to map lithological units and hydrothermal alteration zones and to propose prospective areas for gold mineralization within the western Ahar exploration area, East Azerbaijan Province, Iran. In this research, field-based lithological sampling was integrated with ASTER

* Corresponding author: *E-mail address:* m.shahhosseini@ut.ac.ir (M. Shahhosseini).

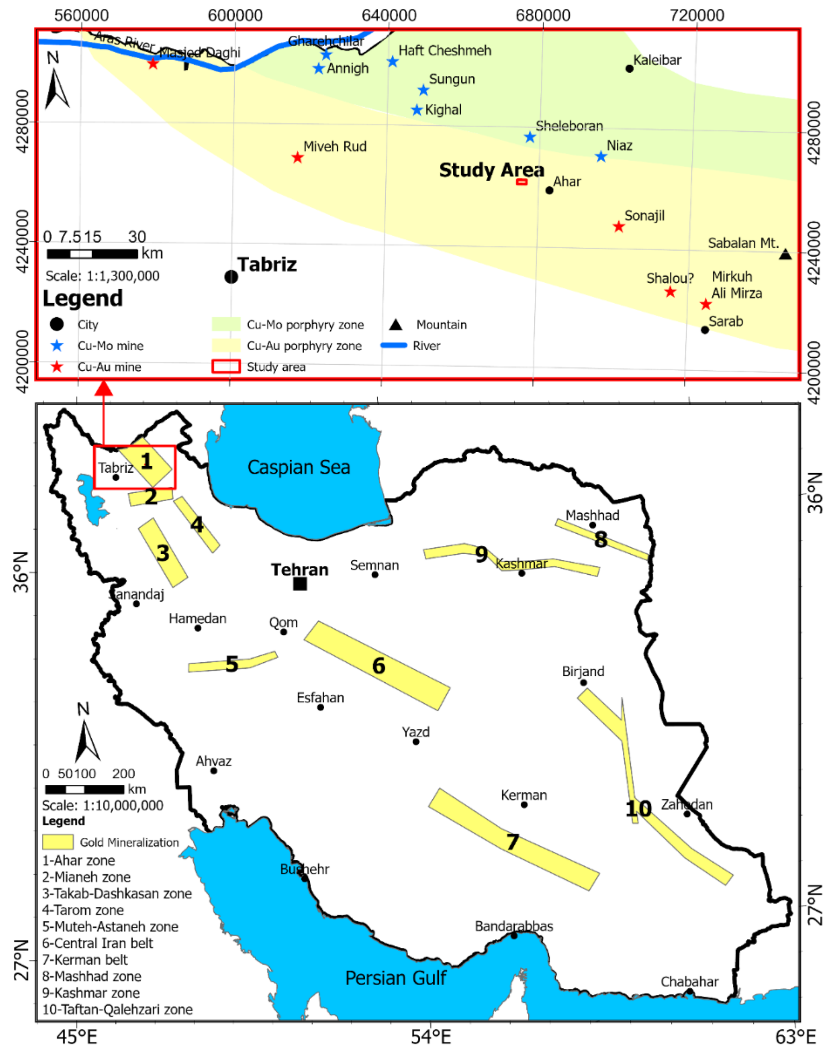


**Figure 1.** Location of the study area relative to the gold-prospective zones of Iran and the copper–gold mineral deposits within the Ahar metallogenic zone (modified after Maghsoudi et al., 2012).

and Landsat 7 satellite data to establish reference spectral signatures. Advanced image processing techniques, including band ratios, false color composites, Principal Component Analysis, and Spectral Angle Mapper, were applied to identify potential zones of gold mineralization.

## 2. Geological setting

The western Ahar exploration area, based on the geological classification of Stocklin (1968), is located within the Central Iran zone, while according to Nabavi's (1976) tectonic subdivision, it belongs to the Alborz–Azerbaijan zone. The exploration area is situated within the Ahar (Arasbaran) metallogenic zone, one of the twenty structural–metallogenic exploration zones defined by the Geological Survey and Mineral Exploration of Iran (GSI). The study area lies within the 1:250,000 Ahar geological map sheet (Babakhani et al., 1990) and the northwestern part of the 1:100,000 Ahar geological map sheet (Mahdavi and Amini Fazl, 1988). The lithology of the Ahar metallogenic zone is predominantly composed of Tertiary magmatic rocks, although older rock units are also exposed in the region. From oldest to youngest, the lithostratigraphic units of the Ahar metallogenic zone include pre–Upper Cretaceous units, Paleocene–Eocene volcano-sedimentary rocks, Oligo–Miocene units, Pliocene igneous–sedimentary rocks, and a Quaternary assemblage of lava flows, pyroclastic deposits, and alluvial sediments (Figure 2). In the Ahar metallogenic zone, the Pre–Upper Cretaceous unit is subdivided into metamorphic rocks and Jurassic–Cretaceous volcano-sedimentary rocks. The metamorphic rocks are exposed in the northern part of Kaleybar and several other locations and consist predominantly of phyllite and marble. The Jurassic–Cretaceous volcano-sedimentary sequence, mainly exposed in the northern part of the 1:250,000 Ahar quadrangle, overlies the metamorphic series. The volcanic and pyroclastic rocks are mainly andesitic, whereas the sedimentary rocks are composed of limestone and marl. The Paleocene–Eocene volcano-sedimentary unit is primarily composed of andesite and is extensively exposed in the northern half as well as in the central part of the Ahar metallogenic zone.

The Oligo–Miocene unit comprises small to large igneous bodies and associated andesitic dikes, as well as alkali-syenite and nepheline-syenite intrusions. Its extrusive equivalents include ignimbrites, dacitic volcanic breccias, and sedimentary rocks such as conglomerates, sandstones, marls, red conglomerates, gypsiferous marls with silt, and alternating sequences of sandstone and silt. These units cover a significant portion of the southern half of the Ahar metallogenic zone. The Pliocene igneous–sedimentary unit includes trachy-andesitic domes, ignimbrites, and volcano-sedimentary sequences with conglomerates, and is exposed in the southern part of the Ahar metallogenic zone, around Varzaqan and south of Sabalan volcano. The Quaternary lavas and pyroclastic deposits are scattered across the southern half of the study area and around Sabalan volcano, particularly south of Meshginshahr, as well as lava and pyroclastic deposits north of Varzaqan. The gold mineralization in the study area is of the intermediate sulfidation epithermal type, typically occurring in continental and island-arc extensional settings. The associated igneous rocks include calc-alkaline rocks, andesite, rhyodacite, and minor rhyolite, while lava and pyroclastic rocks serve as the host. Silver, gold, zinc, lead, copper, and minor amounts of arsenic, molybdenum, and mercury are the associated elements. The orebody exhibits vein, shear, and stockwork forms, with main ore minerals including electrum, acanthite, silver sulfosalts, sphalerite, galena, selenides, and tellurides. Gangue minerals consist of quartz, chalcedony, calcite, and barite, and mineral textures include crustiform, colloform, cockade, and comb structures. Alteration types associated with the deposits include propylitic, sericitic, argillic, and silicic. Near-neutral meteoric and magmatic waters, likely channelled through faults, have contributed to ore formation (Karimpour et al. 1387).

## 3. Materials and methods

The ETM+ sensor, installed on the Landsat 7 satellite, comprises seven reflective bands and one thermal band. The visible and near-infrared bands include bands 1, 2, 3, 4, and 8 (panchromatic), covering a spectral range of 0.45–0.90 µm. The shortwave infrared bands include bands 5 and 7, with a spectral range of 1.55–2.35 µm. The longwave thermal infrared (TIR) band corresponds to band 6, covering 10.4–12.5 µm. Notably, band 8 of ETM+ has a spatial resolution of 15 m (Table 1). With a swath width of 185 km, the ETM+ sensor is widely used in mineral exploration, particularly for the identification of iron oxide minerals.

The ASTER sensor is designed for multispectral imaging, capturing both emitted and reflected electromagnetic radiation from the Earth's surface and atmosphere across fourteen spectral bands. Among these bands, three bands in the visible and near-infrared range (0.52–0.86 µm) have a spatial resolution of 15 m; six bands in the shortwave infrared range (1.6–2.43 µm) have a spatial resolution of 30 m; and five bands in the thermal infrared (TIR) range (8.125–11.65 µm) have a spatial resolution of 90 m. The ASTER sensor, onboard the Terra satellite with a 60 km swath, is widely used for lithology and mineral alteration mapping (Table 1). Indicator minerals of the argillic alteration zone, including kaolinite, illite, montmorillonite, and alunite, exhibit maximum reflection and absorption in ASTER SWIR bands 5–7, while the same minerals show their strongest responses in Landsat 7 bands 5 and 7. Overall, ASTER data provide higher accuracy than Landsat 7 for identifying key alteration minerals, since the wavelength range of Landsat 7 band 7 corresponds to five ASTER SWIR bands (5–9) for reflective data acquisition. Conversely, Landsat 7 contains four bands below 0.9 µm compared to three ASTER VNIR bands, which enhances the detection of iron oxides and hydroxides using Landsat 7 imagery (Table 1).

For ASTER Level 1T data, standard preprocessing began with the aggregation of VNIR and SWIR spectral bands. For both Landsat 7 and ASTER datasets, preprocessing was conducted using the FLAASH model (Fast Line-of-sight Atmospheric Analysis of Spectral Hypercubes) in ENVI software. The FLAASH model corrects for atmospheric effects and converts radiance data to surface reflectance for VNIR and SWIR bands. After applying FLAASH, the spectral alignment of surface pixels was validated for specific features, such as vegetation, using a standard spectral library. For Landsat 7 data, Level 1T spectral data were processed using band combination and band ratio techniques to enhance lithological discrimination.

For ASTER data, band combination, band ratio, Principal Component Analysis, and Spectral Angle Mapper were applied to improve the contrast of both lithological and mineralogical features. The band ratio method involves dividing the Digital Number (DN) values of two bands to generate a grayscale image, enhancing spectral differences that are not distinguishable from individual band analysis (Askari et al., 2018).

Band ratio images provide valuable spectral information for hydrothermal alteration mapping and associated gold mineralization (Abdoulatif et al., 2025; Gabr et al., 2010; Beiranvand Pour & Hashim, 2012; Zoheir et al., 2019). In ASTER spectral data, iron oxides exhibit high reflectance in band 2 and strong absorption in band 1. Therefore, the B2/B1 ratio is used to detect $Fe^{2+}$ and $Fe^{3+}$ oxides in gold exploration (Ninomiya et al., 2005; Beiranvand Pour et al., 2019). According to CSIRO studies, the B5/B4 ratio in porphyry copper–gold deposits highlights iron oxide alteration associated with ferromagnesian silicates, such as biotite, chlorite, and amphibole (Hewson et al., 2005). Hydroxyl-bearing (OH) minerals associated with alteration zones show maximum reflection and absorption in ASTER bands 7 and 9, respectively (Hewson et al., 2005). Quartz exhibits low reflectance in ASTER TIR bands 10 and 12 and high reflectance in band 14. Therefore, the B14/B12 ratio can be applied to detect silicic alteration containing quartz (Rockwell & Hofstra, 2008).

In Landsat 7 ETM+ imagery, hematite shows maximum absorption and reflectance in bands 1 and 3, respectively. Accordingly, the B3/B1 ratio is used to identify hematite and goethite in ETM+ images. To enhance interpretation, band ratios are often combined with false color composites (FCCs). FCC images are effective for detecting vegetation cover, hydrothermal alteration zones, and lithological units (Beiranvand Pour & Hashim, 2012). Principal Component Analysis is a robust and reliable method in image processing that reduces the dimensionality of multispectral datasets by transforming the original, often correlated, spectral bands into a smaller number of uncorrelated output bands (Beiranvand Pour & Hashim, 2012; et al., 2019). This technique simplifies complex spectral data, improves interpretability, and highlights subtle variations in surface materials. PCA has been extensively and successfully applied in ASTER image processing for gold exploration (Beiranvand Pour et al., 2019; Xu et al., 2019; Beiranvand Pour & Hashim, 2012; Zoheir et al., 2019). The Spectral Angle Mapper is an advanced supervised classification technique used to identify minerals and lithological units in a defined area.

This method is based on the concept of the spectral angle, which measures the angle between two spectral vectors in an n-dimensional spectral space (Rashmi et al., 2014). The angle is computed between the spectral vector of each pixel and a reference spectral vector. A smaller angle indicates greater similarity, and only pixels within a predefined threshold are classified. Reference spectra for SAM classification are derived from laboratory analyses, field measurements, or directly from imagery. In this study, the final spectra were determined from the average spectra of the regions of interest (ROIs) and prepared using ASCII files or spectral libraries. Specifically, kaolinite and chlorite were selected as reference minerals and identified using the USGS spectral library. The SAM method, applied to ASTER sensor data, is widely used for classification and mapping of hydrothermal alteration zones in gold exploration (Sheikhrahimi et al., 2019; Beiranvand Pour & Hashim, 2012). The results of lithological and alteration classification based on Landsat 7 and ASTER image processing were validated through field investigations, including targeted rock sampling. Petrographic, mineralogical, and geochemical analyses were conducted on the collected samples. The outcomes of satellite image processing, field data, geochemical analyses, and GIS datasets were integrated to produce the hydrothermal alteration map.

## 4. Results and discussion

### *4.1. Vegetation highlighting*

The widely used Normalized Difference Vegetation Index (NDVI) is calculated as the ratio of the difference between ASTER bands 3 and 2 to their sum. This index is commonly applied for vegetation studies using atmospherically corrected ASTER reflectance data (Ninomiya, 2003). In grayscale NDVI images, bright pixels correspond to areas of dense vegetation (Figure 3). Very limited vegetation is observed in the southwestern corner of the study area. In ETM+ data, vegetation shows maximum reflectance in band 4 and minimum reflectance in bands 1 and 7. Considering the correlation between these bands, a false color composite (FCC) of bands 7, 4, and 1 (RGB = 741) was used to highlight vegetation. In this FCC, band 4 is assigned to green, which corresponds

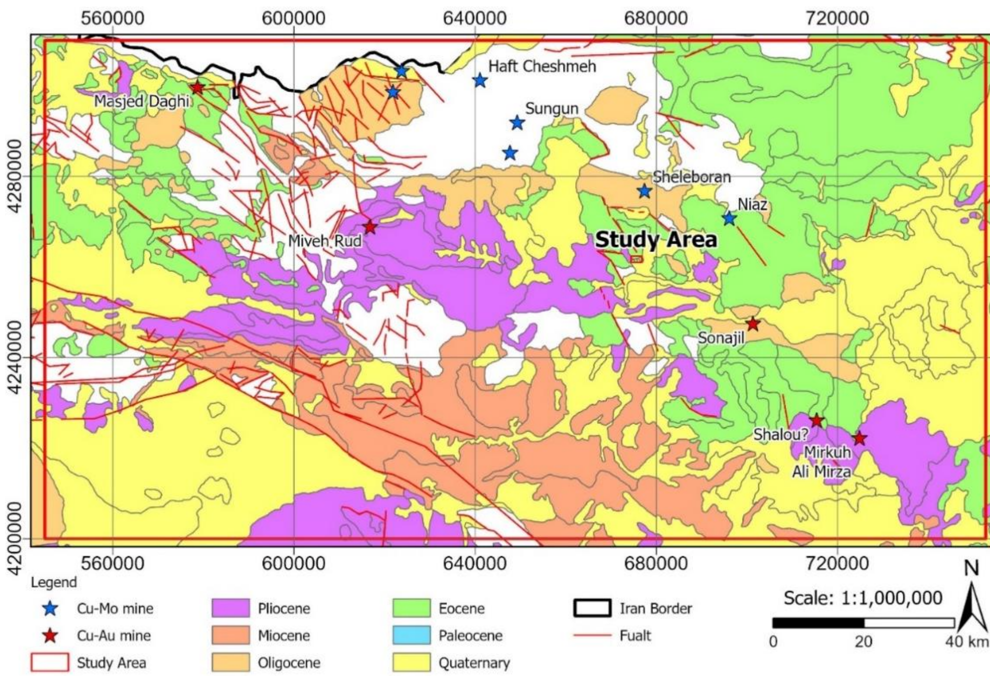


**Figure 2.** Geological periods of Tertiary-aged rock units surrounding the study area within the Ahar metallogenic zone.

**Table 1.** Comparison of the wavelength ranges of ETM+ and ASTER sensor bands.

| Sensor | Subsystem | Band Number | Spectral Range (µm) | Ground Resolution (m) | Swath Width (km) | Year of Launch |
|---|---|---|---|---|---|---|
| Landsat7 ETM+ | VNIR | 1-Blue | 0.45-0.52 | 30 | 185 | 1999 |
| | | 2-Green | 0.52-0.6 | 30 | | |
| | | 3-Red | 0.63-0.69 | 30 | | |
| | | 4-NIR | 0.77-0.9 | 30 | | |
| | SWIR | 5-SWIR1 | 1.55-1.75 | 30 | | |
| | TIR | 6-Thermal | 10.4-12.5 | 60* (30) | | |
| | SWIR | 7-SWIR2 | 2.09-2.35 | 30 | | |
| | VNIR | 8-Panchromatic | 0.52-0.9 | 15 | | |
| TERRA ASTER | VNIR | 1-Green | 0.52-0.6 | 15 | 60 | 1999 |
| | | 2-Red | 0.63-0.69 | 15 | | |
| | | 3N | 0.78-0.86 | 15 | | |
| | | 3B | 0.78-0.86 | 15 | | |
| | SWIR | 4 | 1.6-1.7 | 30 | | |
| | | 5 | 2.145-2.185 | 30 | | |
| | | 6 | 2.185-2.225 | 30 | | |
| | | 7 | 2.235-2.285 | 30 | | |
| | | 8 | 2.295-2.365 | 30 | | |
| | | 9 | 2.36-2.43 | 30 | | |
| | TIR | 10 | 8.125-8.475 | 90 | | |
| | | 11 | 8.475-8.825 | 90 | | |
| | | 12 | 8.925-9.275 | 90 | | |
| | | 13 | 10.25-10.95 | 90 | | |
| | | 14 | 10.95-11.65 | 90 | | |

to the highest reflectance of vegetation. Consequently, sparse vegetation in the southwestern corner appears light green (Figure 3). The vegetation mapping results from ETM+ FCC 741 are consistent with those obtained from NDVI, confirming that vegetation does not significantly interfere with the detection of surface features, particularly alteration halos, in the study area.

### *4.2. Fault and lineament highlighting*

The identification of faults and lineaments is of critical importance in mineral exploration, particularly for vein-type deposits. Fault intersections in porphyry and massive sulfide deposits are associated with high mineralization potential. To enhance the detection of lineaments in the study area, directional filters at 45° and 315° were applied to ASTER satellite imagery (Figure 4). Fault density is highest along the NW–SE and NE–SW trends. In addition to these two dominant orientations, several E–W lineaments were also observed in the central and southern parts of the study area. The effectiveness of directional filters in highlighting lineaments can be validated against the 1:100,000-scale geological map of Ahar, where a confirmed thrust fault trending NW–SE exists within the study area. This comparison confirms the capability of the directional filters to accurately detect faults.

The thrust fault operates within a compressional tectonic regime and is unlikely to exert a direct control on the migration of ore-forming

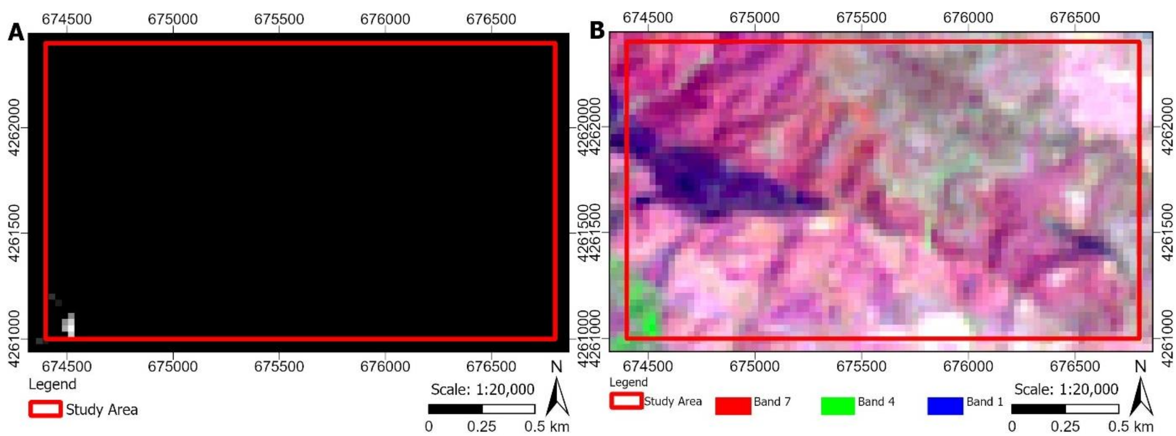


**Figure 3.** Vegetation cover of the study area based on: A) bright pixels in the NDVI image, and B) green color in the ETM+ false color composite (bands 7, 4, 1; RGB = 741).

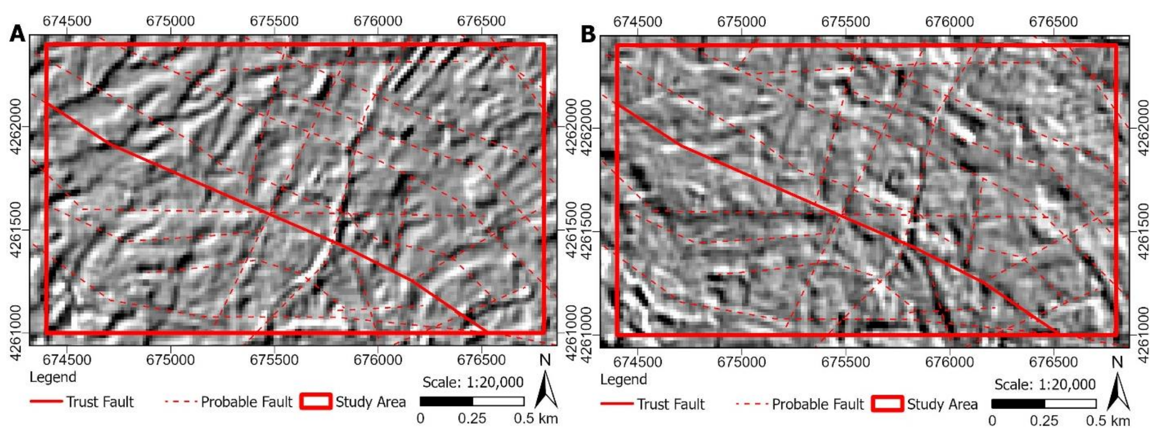


**Figure 4.** Probable faults in the study area identified using directional filters: A) 45° and B) 315°.

fluids into the study area. Nonetheless, the regional activity of the thrust fault has induced the development of a network of normal faults within an extensional system, particularly those oriented parallel to the thrust fault. Extensional faults are therefore considered to play a primary role in facilitating the transport of mineralizing fluids into the study area. The spatial association of hydrothermal alteration with these extensional faults is noteworthy and indicates their significance in localizing mineralization.

### *4.3. Alteration highlighting*

To detect iron oxides in the study area, the B2/B1 band ratio of ASTER imagery was applied. The highest abundance of $Fe^{2+}$ and $Fe^{3+}$ oxides was observed in the northwestern and western parts of the study area, trending approximately NW–SE (Figure 5). Using the B3/B1 band ratio of ETM+ imagery, hematite appears as bright pixels in the northern and western sections of the area (Figure 5). The occurrence of iron oxides in ASTER images not only confirms the results from ETM+ but also provides better discrimination and greater spatial extent of iron oxide zones.

Based on the B5/B4 band ratio in ASTER imagery, iron oxides associated with ferromagnesian silicates exhibit limited spatial distribution in the western part of the study area (Figure 6). The B7/B9 band ratio was used to detect hydroxyl-bearing (OH) minerals in ASTER images. These minerals were observed in association with most alteration types and were widely distributed across the study area, indicating intense hydrothermal alteration (Figure 6). To highlight silicic alteration containing quartz, the B14/B12 band ratio of ASTER imagery was applied (Figure 6). In the resulting image, silicic units without ferromagnesian minerals were clearly delineated. This B14/B12 ratio image shows limited similarity with the B5/B4 ratio image. The B14/B12 ratio effectively maps felsic rocks with high silica content, silicic caps, and quartz veins, particularly in the northwestern and southeastern parts of the study area. Using a single spectral band provides limited information for the identification of lithological units and alteration zones. Therefore, by considering the different wavelengths and spectral behavior of the target features, appropriate band combinations are selected. For ETM+ imagery, a false-color composite using band ratios B3/B1 (red), B3/B5 (green), and B5/B7 (blue) is an effective combination for highlighting lithological variations. Based on color differentiation, four lithological units—green, gray, reddish-orange, and orange—can be identified in the study area (Figure 7). For ASTER imagery, the following false color composites are considered the most effective for mapping alteration zones associated with porphyry copper and epithermal gold deposits: RGB = 4-6-8 (bands 4, 6, 8), RGB = 4-5-7 (bands 4, 5, 7), RGB = 7-2-9 (bands 7, 2, 9) (Azizi et al., 2010; Blocki and Pourmirzaei, 2009). Argillic and sericitic alteration minerals exhibit high reflectance in band 4 and thus appear red to pink in the 4-6-8 composite, highlighting argillic-sericitic zones trending NW–SE, which are observed throughout much of the study area (Figure 7). Propylitic alteration minerals, with high reflectance in bands 5 and 6, appear dark green in the 4-6-8 composite and indicate propylitic zones which are widespread in the northern and eastern parts of the study area (Figure 7). In the 4-5-7 ASTER composite, red to pink colors represent argillic alteration, confirming the results observed in the 4-6-8 composite. Additionally, the 7-2-9 ASTER composite effectively highlights sericitic and argillic alteration, with relatively extensive zones appearing light green in the northeastern, eastern, and southern parts of the study area (Figure 7).

A correlation matrix was used to extract eigenvectors and eigenvalues. Muscovite, as an indicator mineral of sericitic alteration, exhibits the highest reflectance and absorption in ASTER bands 7 and 6, respectively. Principal Component 7 (PC7), which shows the largest contrast between the eigenvalues of bands 7 and 6, was selected to represent sericitic alteration. Sericitic alteration is widespread throughout the study area, particularly in the northwestern and southern sections (Figure 8).

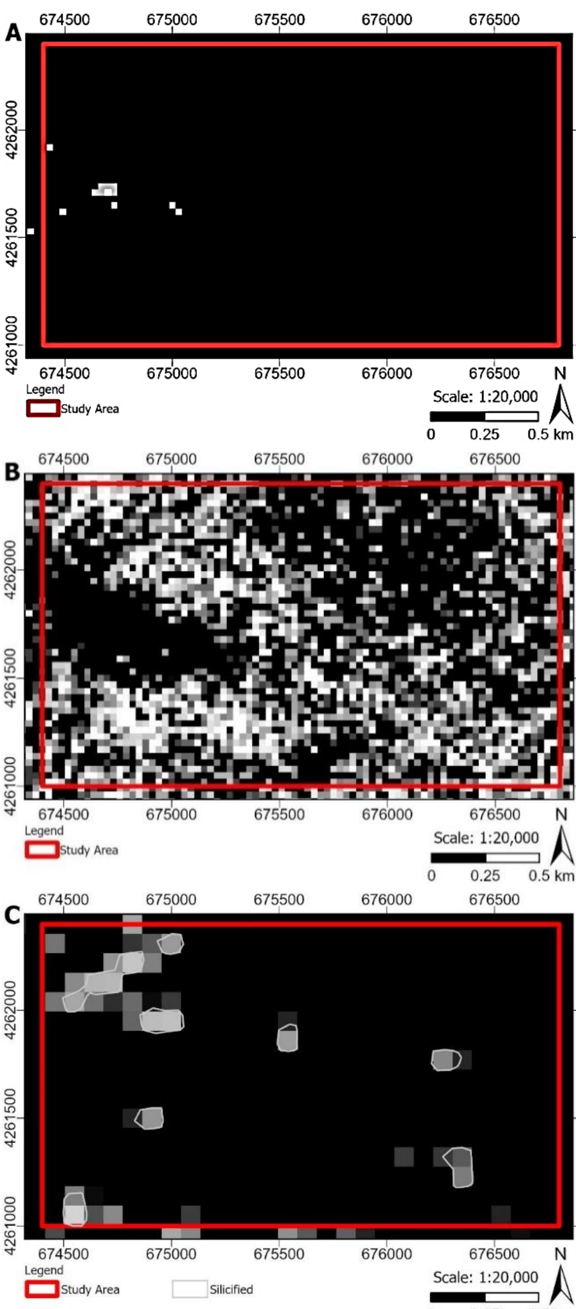


**Figure 6.** Distribution of minerals (bright pixels) in the study area based on ASTER band ratios: A) iron oxides associated with ferromagnesian silicates (B5/B4), B) hydroxyl-bearing (OH) minerals (B7/B9), and C) acidic silicates such as quartz (B14/B12).

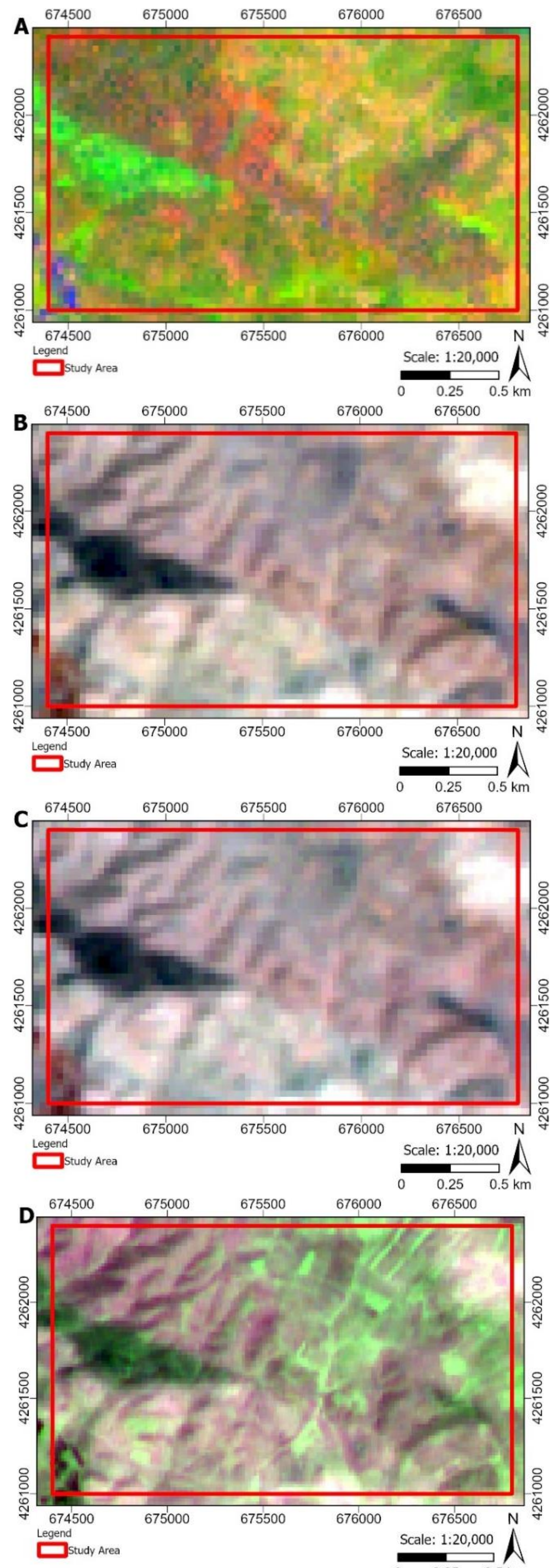


**Figure 7.** False color composites in the study area: A) ETM+ B3/B1–B3/B5–B5/B7, B) ASTER 4-6-8 highlighting argillic–sericitic alteration (red to pink pixels), C) ASTER 4-5-7 highlighting argillic–sericitic alteration (red to pink pixels), and D) ASTER 7-2-9 highlighting sericitic–argillic alteration (light green pixels).

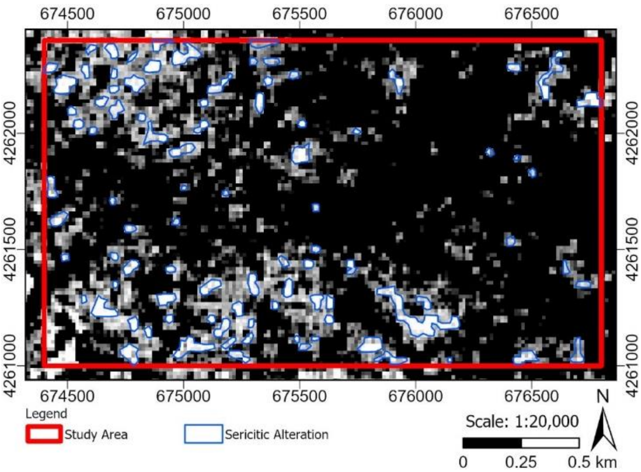


**Figure 8.** Extent of sericitic alteration (bright pixels) in the study area based on PC7 derived from ASTER imagery.

Kaolinite, as the indicator mineral of argillic alteration, exhibits high reflectance in ASTER band 4, while chlorite, the indicator mineral of propylitic alteration, shows high reflectance in bands 5 and 6. Based on the results of false color composites for highlighting argillic and propylitic alteration, validated reference spectra for kaolinite and chlorite were selected within the study area (Figures 9 and 10). Supervised classification using the Spectral Angle Mapper method was applied to support field mapping and petrographic and mineralogical analyses. SAM is particularly effective in complex geological environments, enhancing spatial accuracy for the identification of promising gold mineralization zones.

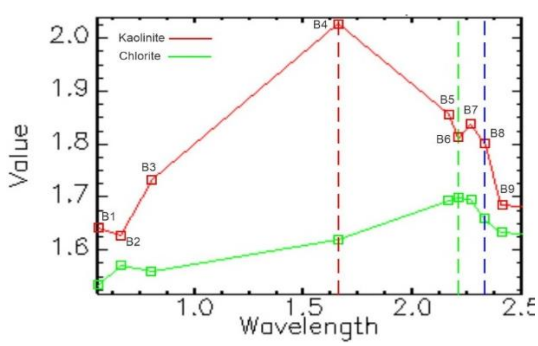


**Figure 9.** Reflectance spectra of reference minerals kaolinite (red) and chlorite (green) from the ground surface in ASTER imagery for the study area.

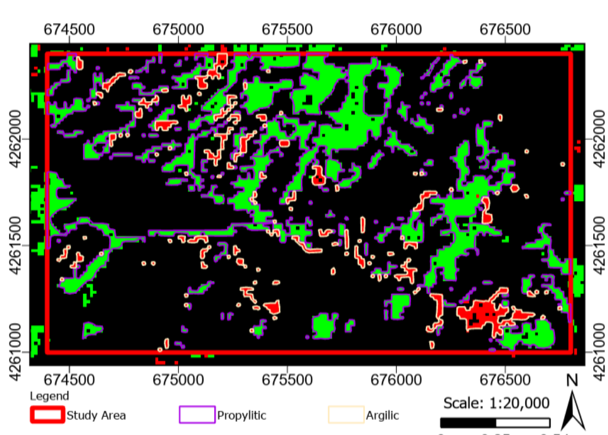


**Figure 10.** Distribution of argillic and propylitic alteration in the study area based on the Spectral Angle Mapper method applied to ASTER imagery.

### *4.4. Field validation*

To validate the remote sensing interpretations, petrographic analysis was conducted on five representative rock samples (KT02, KT04, KT05, KT08, and KT09), including metarhyolite and tuff. The main objective was to confirm the mineralogical composition and assess the degree of silicic, sericitic, propylitic, and argillic alteration in the rocks of the study area. Thin-section analyses were performed using a polarized light microscope (Figure 11a–d).

The metarhyolite samples are volcanic igneous rocks with a silicic and felsic composition. Samples KT02 and KT05 fall within the rhyolitic compositional range. Sample KT02 has undergone intense silicification, resulting in almost complete alteration of the primary minerals and the original texture (Figure 11). Quartz grains of varying sizes, occurring as cement and anhedral to subhedral fragments, constitute the main component of the sample. In some areas, pseudomorphs of primary feldspars are barely discernible. Fine opaque and sericite particles are also sporadically present. Dispersed patches of iron-bearing phases, such as hematite and goethite, are observable throughout the sample. The texture and mineral composition of sample KT05 are largely similar to those of KT02.

Quartz, occurring as cryptocrystalline and crystalline varieties, forms the groundmass and the majority of the fragments (Figure 11). Intense silicification has led to near-complete replacement of the primary minerals by silica, leaving only minor subhedral feldspar remnants. In some parts, impregnation by iron oxides has caused the rock to appear dark brown. Interstitial spaces between the quartz fragments and feldspar remnants contain very fine-grained mica, sericite, and, occasionally, calcite. The crystal-vitric tuff samples are fine-grained pyroclastic igneous rocks. Sample KT04 represents a highly silicified tuff. In the less silicified portions, the primary rock is very fine-grained and contains ash-sized particles, devitrified glass, very fine quartz crystals, alkali feldspar, small biotite flakes, and minor plagioclase. Multiple, intertwined veins of varying thickness cut the rock in a network-like pattern, locally producing a shear texture. Quartz, occurring in both microcrystalline and coarse-grained forms, constitutes the main component of the veins. In some veins, barite occurs as bladed crystals, either alone or associated with quartz. The presence of barite in combination with silicification suggests a potential genetic link between this rock unit and mineralization.

The dominant alteration in the sample is intense silicification. Lithic tuff samples represent pyroclastic rocks belonging to the subgroup of fragment-rich tuffs. In sample KT09, the interstitial spaces between lithic fragments are filled with microcrystalline silica, clay minerals, very fine mica flakes, and calcite grains (Figure 11). Rarely, fragmented quartz and feldspar crystals are also observable. The lithic fragments predominantly exhibit a microlitic to flow texture, and less commonly a micro-porphyritic texture, with compositions ranging from andesitic basalt, basalt, and rhyodacite to occasional andesite. The sample is primarily composed of lithic fragments with a minor proportion of cement. Most lithic fragments have undergone minimal alteration, with plagioclase being the most abundant unaltered mineral in the sample. Coarse calcite grains are present sporadically, occasionally filling voids and fractures. Sublithic arenites are clastic sedimentary rocks classified within the sandstone subgroup based on grain size. In sample KT08, a high diversity of mineral and lithic fragments with varying compositions is observed (Figure 11). Quartz, occurring as sub-rounded to angular grains, is the most abundant constituent of the rock. Scattered grains of plagioclase, alkali feldspar, and mica flakes—particularly biotite—are also present within the sample. The lithic fragments comprise chert, tuff, and volcanic igneous rocks including andesitic basalt, diabase, and siltstone. The interstitial cement is predominantly silica.

### *4.5. Geochemical study of gold mineralization*

In this study, gold mineralization exhibits a close spatial association with zones of abundant silica and quartz veins. Field sampling for geochemical and petrographic analysis revealed evidence of silicification, propylitic alteration, and iron oxide enrichment (Figure

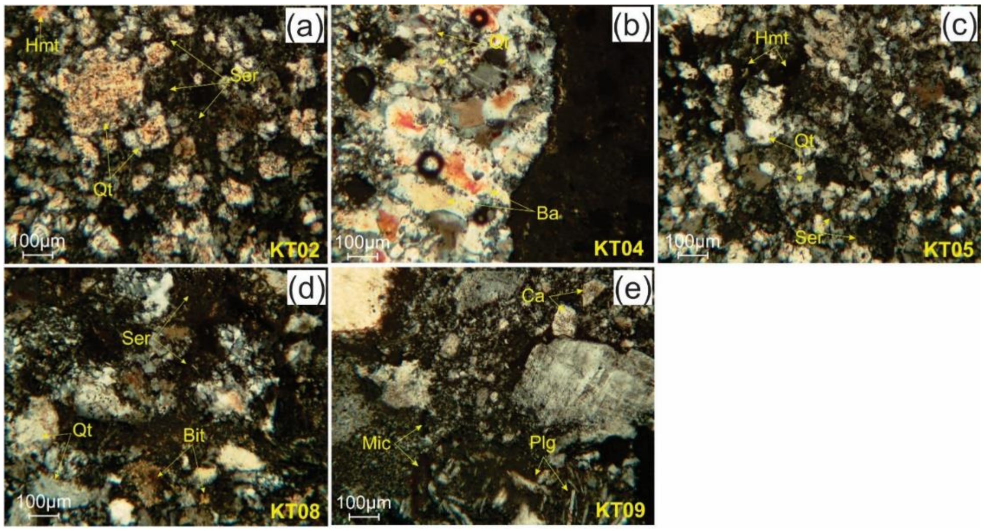


**Figure 11.** Thin-section images of samples a) KT02, b) KT04, c) KT05, d) KT08, e) KT09. Mineral abbreviations: Ca = calcite, Plg = plagioclase, Hmt = hematite, Ser = sericite, Bit = biotite, Qt = quartz, Mic = mica, Ba = barite.

12). Quartz veins were observed to occur in close spatial proximity to barite veins. A total of six rock samples were collected from outcrops of quartz and quartz–barite veins, with particular attention to areas of potential gold mineralization (Figure 12). Gold concentrations determined by Fire Assay in samples KF01, KF02, KF05, KF06, KF20, and KF29 were 0.021, 0.276, 3.138, 0.911, 0.932, and 1.212 g/t, respectively. In the 1:20,000 scale alteration map of western Ahar, locations of gold mineralization were found to closely correlate with silicic, sericitic, argillic, and iron oxide alterations (Figure 13). Integrating spectral, structural, petrographic, and field data within a spatial multi-criteria decision-making framework (Analytic Hierarchy Process, AHP) provides a robust approach for modeling the potential of gold mineralization.

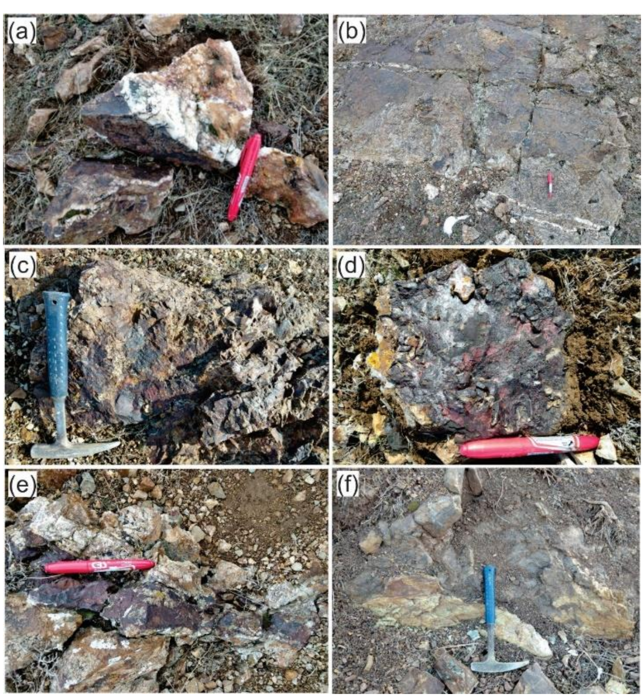


**Figure 12.** Field sampling images showing evidence of alteration and gold mineralization outcrops: a) Coarse-grained quartz with geode concentrations, b) Quartz and barite veins in andesite, c) Iron oxide alteration in volcanic breccia, d) Iron oxide alteration with goethite, hematite, and limonite in volcanic breccia, e) Barite–quartz–iron oxide vein, f) Propylitic alteration with chlorite and epidote minerals.

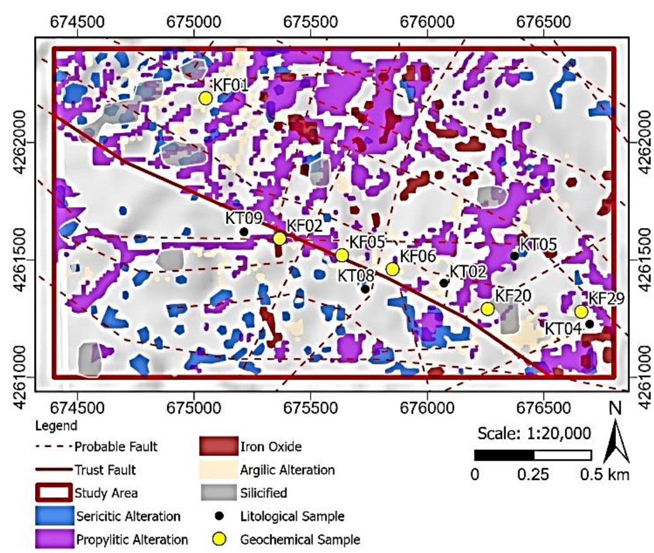


**Figure 13.** Alteration map of the West Ahar area at a 1:20,000 scale.

## 5. Conclusions and recommendations

The integrated application of ASTER and Landsat 7 image processing for producing a 1:20,000-scale alteration map and exploring gold mineralization in the West Ahar region was successfully demonstrated. The use of ASTER multispectral imagery, processed through band ratioing, false-color composites, principal component analysis, and spectral angle mapping, proved effective in distinguishing and mapping various alteration types associated with gold mineralization. The identification of silicic, sericitic, argillic, and iron oxide alterations, validated through field investigations and petrographic studies, indicates that gold mineralization in West Ahar is related to hydrothermal fluids. Mapping faults and lineaments provided insights into the pathways of fluid migration in the study area. The region is characterized by Paleocene–Late Eocene extrusive and pyroclastic igneous rocks, including andesite, andesitic basalt, basalt, tuff, and meta-rhyolite. Additionally, Paleocene chemical and clastic sedimentary rocks, including purple conglomerates with fossils, sedimentary layers, fossiliferous limestone, and sandstones, are present. The framework proposed in this study offers a cost-effective, rapid, and straightforward approach for exploring target mineralization, particularly for the strategic element gold.

## References


[1]. Abdoulatif, A., Saley, M., & Mohamed, M. (2025). Mapping of hydrothermal alteration minerals related to Tongue Tonguey (Sirba, Niger) gold mineralization using Landsat 8 OLI data and remote sensing. *Asian Journal of Physical and Chemical Sciences, 13*, 1–14.

[2]. Askari, G., Pour, A. B., Pradhan, B., Sarfi, M., & Nazemnejad, F. (2018). Band ratios matrix transformation (BRMT): A sedimentary lithology mapping approach using ASTER satellite sensor. *Sensors, 18*, 3213.

[3]. Azizi, H., Tarverdi, M. A., & Akbarpour, A. (2010). Extraction of hydrothermal alterations from ASTER SWIR data from east Zanjan, northern Iran. *Advances in Space Research, 46*, 99–109.

[4]. Babakhani, A. R., Lescuyer, L., & Rieu, R. (1990). *Explanatory text of the Ahar quadrangle geological map (Scale 1:250,000)*. Geological Survey of Iran.

[5]. Bedini, E. (2019). Application of WorldView-3 imagery and ASTER TIR data to map alteration minerals associated with the Rodalquilar gold deposits, southeast Spain. *Advances in Space Research, 63*, 3346–3357.

[6]. Beiranvand Pour, A., & Hashim, M. (2012). The application of ASTER remote sensing data to porphyry copper and epithermal gold deposits. *Ore Geology Reviews, 44*, 1–9.

[7]. Beiranvand Pour, A., Park, T.-Y. S., Park, Y., Hong, J. K., Muslim, A. M., Läufer, A., Crispini, L., Pradhan, B., Zoheir, B., Rahmani, O., Hashim, M., & Hossain, M. S. (2019). Landsat-8, ASTER, and WorldView-3 multispectral satellite imagery for prospecting copper-gold mineralization in NW Greenland. *Remote Sensing, 11*, 2430. https://doi.org/10.3390/rs11202430

[8]. Boloki, M., & Poormirzaee, R. (2009). Using ASTER image processing for hydrothermal alteration and key alteration minerals mapping in Siyahrud area, Iran. *International Journal of Geology, 3*, 38–43.

[9]. Gabr, S., Ghulam, A., & Kusky, T. (2010). Detecting areas of high-potential gold mineralization using ASTER data. *Ore Geology Reviews, 38*, 59–69.

[10]. Ghorbani, M. (2002). *Introduction to economic geology of Iran* (Report No. 2). National Database of Earth Sciences.

[11]. Ghorbani, M. (2008). *Economic geology of ore deposits and mineral indicators in Iran*. Arin Zamin Publications.

[12]. Hewson, R. D., Cudahy, T., Mizuhiko, S., Ueda, K., & Mauger, A. J. (2005). Seamless geological map generation using ASTER in the Broken Hill-Curnamona province of Australia. *Remote Sensing of Environment, 99*(1–2), 159–172.

[13]. Karimpour, M. H., Malekzadeh, A., & Heydarian, M. R. (1387). *Ektesaf-e zakhayer-e ma'dani: Modelhaye zaminshenasi, geochemistry, mahvarei va geophysiki* [Exploration of mineral deposits: Geological, geochemical, satellite, and geophysical models]. Ferdowsi University of Mashhad Press. (in Persian)

[14]. Maghsoudi, A., Yazdi, M., Mehrpartou, M., Vosoughi, M., & Younesi, S. (2012). Porphyry Cu–Au mineralization in the Mirkuh Ali Mirza magmatic complex, NW Iran. *Journal of Asian Earth Sciences*. https://doi.org/10.1016/j.jseaes.2012.10.002

[15]. Mahdavi, A., Amini Fazl, A., & Alavi Tehrani, N. (1988). *Ahar geological map (Scale 1:100,000)*. Geological Survey and Mineral Exploration of Iran.

[16]. Nabavi, M. H. (1976). *An introduction to the geology of Iran*. Geological Survey of Iran.

[17]. Ninomiya, Y. (2003). A stabilized vegetation index and several mineralogic indices defined for ASTER VNIR and SWIR data. In *Proceedings of IEEE 2003 International Geoscience and Remote Sensing Symposium (IGARSS'03)* (Vol. 3, pp. 1552–1554).

[18]. Ninomiya, Y., Fu, B., & Cudahy, T. J. (2005). Detecting lithology with advanced spaceborne thermal emission and reflection radiometer (ASTER) multispectral thermal infrared radiance-at-sensor data. *Remote Sensing of Environment, 99*, 127–139.

[19]. Rani, K. (2025). Mineral exploration using remote sensing. In *Remote sensing for geophysicists* (pp. 79–94). CRC Press.

[20]. Rashmi, S., Addamani, S., & Ravikiran, A. (2014). Spectral angle mapper algorithm for remote sensing image classification. *International Journal of Innovative Science, Engineering and Technology, 1*, 5481–5490.

[21]. Rockwell, B. W., & Hofstra, A. H. (2008). Identification of quartz and carbonate minerals across northern Nevada using ASTER thermal infrared emissivity data: Implications for geologic mapping and mineral resource investigations in well-studied and frontier areas. *Geosphere, 4*(1), 218–246.

[22]. Sabins, F. F. (1999). Remote sensing for mineral exploration. *Ore Geology Reviews, 14*, 157–183.

[23]. Sheikhrahimi, A., Beiranvand Pour, A., Pradhan, B., & Zoheir, B. (2019). Mapping hydrothermal alteration zones and lineaments associated with orogenic gold mineralization using ASTER data: A case study from the Sanandaj-Sirjan Zone, Iran. *Advances in Space Research, 63*, 3315–3332. https://doi.org/10.3390/rs11121450